

**Accelerating frequency-domain numerical methods for weakly nonlinear focused  
ultrasound using nested meshes**

Samuel P. Groth,<sup>1, a</sup> Pierre G  lat,<sup>2</sup> Seyyed R. Haqshenas,<sup>2</sup> Nader Saffari,<sup>2</sup> Elwin van 't  
Wout,<sup>3</sup> Timo Betcke,<sup>4</sup> and Garth N. Wells<sup>1</sup>

<sup>1</sup>*Department of Engineering, University of Cambridge, Cambridge CB2 1PZ,  
United Kingdom*

<sup>2</sup>*Department of Mechanical Engineering, University College London,  
London WC1E 7JE, United Kingdom*

<sup>3</sup>*Institute for Mathematical and Computational Engineering, School of Engineering  
and Faculty of Mathematics, Pontificia Universidad Cat  lica de Chile, Santiago,  
Chile*

<sup>4</sup>*Department of Mathematics, University College London, London WC1H 0AY,  
United Kingdom*

(Dated: 22 April 2021)

1 The numerical simulation of **weakly** nonlinear ultrasound is important in treatment  
 2 planning for **focused ultrasound (FUS)** therapies. However, the large domain sizes  
 3 and generation of higher harmonics at the focus make these problems extremely com-  
 4 putationally demanding. Numerical methods typically employ a uniform mesh fine  
 5 enough to resolve the highest harmonic present in the problem, leading to a very large  
 6 number of degrees of freedom. This paper proposes a more efficient strategy in which  
 7 each harmonic is approximated on a separate mesh, the size of which is proportional  
 8 to **the** wavelength of the harmonic. The increase in resolution required to resolve a  
 9 smaller wavelength is balanced by a reduction in the domain size. This nested mesh-  
 10 ing is feasible owing to the increasingly localised nature of higher harmonics near the  
 11 focus.

12 Numerical experiments are performed for **FUS** transducers in homogeneous media  
 13 in order to determine the size of the meshes required to accurately represent the har-  
 14 monics. In particular, a fast *volume potential* approach is proposed and employed to  
 15 perform convergence experiments as the computation domain size is modified. This  
 16 approach allows each harmonic to be computed via the evaluation of an integral over  
 17 the domain. Discretising this integral using the midpoint rule allows the computa-  
 18 tions to be performed rapidly with the FFT. It is shown that at least an order of  
 19 magnitude reduction in memory consumption and computation time can be achieved  
 20 with nested meshing. **Finally, it is demonstrated how to generalise this approach to**  
 21 **inhomogeneous propagation domains.**

---

<sup>a</sup>[samuelpgroth@gmail.com](mailto:samuelpgroth@gmail.com)

## I. INTRODUCTION

**Focused ultrasound (FUS)** is a non-invasive tumor ablation therapy in which acoustic waves are focused at a target location, thereby elevating the temperature sufficiently to destroy the tumor tissue. Tissue death can be caused directly via thermal ablation, or via other mechanisms such as cavitation (Izadifar *et al.*, 2017; Vlaisavljevich *et al.*, 2013), **shock-scattering histotripsy** (Maxwell *et al.*, 2011), and **boiling histotripsy** (Khokhlova *et al.*, 2011). In the thermal ablation setting, which is the focus of this article, the peak acoustic pressure is often between 1 and 10 MPa, at which linear acoustic theory is no longer accurate. Indeed it has been observed that the contributions from nonlinear effects can increase the temperature at the focal point by an additional 20%, thus substantially reducing the time required for ablation when compared to simulations using linear theory (Solovchuk *et al.*, 2014). To simulate the nonlinear acoustic field, a popular model is the Westervelt equation, which incorporates a quadratic pressure term. Numerically solving the Westervelt equation in a **FUS** setting is computationally challenging since the domains are large compared to the smallest wavelength present.

To put into context the scale of the computational problems presented by **FUS**, consider a bowl-shaped **FUS** transducer with radius 7.5cm and geometric focal length 15cm operating at 1.1MHz. Transducers of this size are suitable for deep-seated tumors, located in the liver, for example. A simulation domain spanning the face of the bowl and extending to the focal region is approximately 100 wavelengths across in each dimension. If there are five harmonics present in the nonlinear field, then this is five hundred wavelengths at the fifth

harmonic. In order to obtain a reasonable accuracy level, we can assume that at least six degrees of freedom (DOF) per wavelength are required (Marburg, 2008). Then to simulate this problem in three dimensions, we would require 27 billion degrees of freedom. Handling such a large system presents an enormous computational load in terms of memory and time.

There has been a great deal of research effort aimed at reducing the computational cost of nonlinear FUS simulations. Much of this work employs at least one simplifying assumption, such as axisymmetry, one-way wave propagation, or the parabolic approximation (see (Gu and Jing, 2015) for a review). The most popular methods for solving the original Westervelt equation (or equivalent) are the finite-difference time-domain method (Solovchuk *et al.*, 2013) (FDTD) and the  $k$ -space pseudospectral method (Treeby *et al.*, 2012) (KSPS). Although powerful techniques, these full-wave solvers can still yield simulation times in excess of a day for realistic problems when run on a large cluster (Jaros *et al.*, 2016).

In this paper, we set out to improve upon the meshing strategies employed in the popular full-wave solvers, namely uniform meshes resolved according to the wavelength of the highest harmonic. Such a meshing approach is inefficient since the higher harmonics are localised around the focus, therefore the extremely fine mesh far away from the focus is likely overkill. It seems intuitive that a mesh that is gradually refined as the focus is approached would be sensible, but at what rate? And what saving can one expect to achieve? Here we address these questions via numerical experimentation on realistic FUS transducers taken from (Sonic Concepts, Accessed: 2020-08-19).

We note similar strategies have previously been employed to reduce the computational load of nonlinear acoustics simulations (Karzova *et al.*, 2017; Yuldashev and Khokhlova,

2011). In these prior works, it was also observed that far from the transducer focus, higher harmonics provide negligible contributions to the acoustic field and therefore, to save on storage requirements, higher harmonics are stored only on smaller domains, centred at the focus. However, the grid step used in these works is not altered for the different harmonic computations. By increasing the grid step for lower harmonics, further computational savings can be achieved, as we demonstrate in this article. Furthermore, we detail an in-depth study of how to choose appropriate computational domains for each harmonic and we provide a useful rule of thumb relating the domain dimensions to each harmonic’s wavelength.

In order to perform these experiments efficiently, we consider a simplified setting in which the propagation medium is homogeneous and the signal is assumed to have harmonic time dependence. Furthermore, we consider settings in which the peak amplitude is no more than 15MPa and thus the field is only weakly non-linear. Under the time-harmonic and weakly non-linear assumptions, the full-wave Westervelt equation reduces to a series of inhomogeneous Helmholtz equations, one for each harmonic present in the field (as in, e.g., (Du and Jensen, 2013)). We note that the weak non-linearity permits us to reasonably neglect the transfer of energy from higher to lower harmonics. This is, however, not valid for extremely high amplitude fields, as encountered in histotripsy applications.

Since we consider a homogeneous medium, each Helmholtz equation is exactly solved by the evaluation of the appropriate *volume potential* integral (Costabel, 2015). Therefore, for each harmonic in the field, we look at the convergence of the volume potential as the domain of integration is increased. In order to efficiently evaluate the volume potential, we discretise the domain over a uniform voxel mesh, which allows the summation (i.e., the discrete form

of the integration) to be performed rapidly using the fast-Fourier transform (FFT). This is an extremely efficient technique for computing high-order harmonics in a homogeneous medium and its application in this area is, to the best of the authors' knowledge, novel.

For numerical investigations with different transducer configurations and within two different media (water and liver), we deduce that (for the configurations considered) in order to perform accurate computations of the second harmonic, the computation domain must extend all the way back to the transducer, however may be contracted slightly in the transverse direction. For the third and higher harmonics, the computation domain may be contracted in both the axial and transverse directions, thus leading to substantial computational savings. In fact, we demonstrate that an accurate approximation (less than 1% relative error) may be obtained while contracting the width and length of the domain in proportion to the wavelength of the harmonic. Thus the number of cells in every mesh is roughly equal. This amounts to a reduction in the number of DOF by a factor of approximately  $(n/2)^3$ , where  $n$  is the number of harmonics being computed.

In practice, this leads to a series of nested meshes, each at the resolution required for the appropriate harmonic and all with the same number of voxels. To perform computations for higher harmonics, solutions from lower harmonics are interpolated onto the finer meshes. We outline an algorithm for this more efficient computation of all the harmonics in Section VI and examine its performance.

The layout of the paper is as follows. Section II outlines the mathematical model we employ for our FUS setup. In particular we consider the Westervelt equation and review how it reduces to a series of Helmholtz equations under the time-harmonic assumption. We further

simplify the equations via an assumption of weak nonlinearity, which is valid for a large range of ?? transducer settings. In Section III we describe how, in the homogeneous domain case, the Helmholtz equations are solved exactly via volume potentials. It is then described how these volume potentials are efficiently approximated using a voxelised discretisation approach. This leads to the discrete versions of the volume potentials having block-Toeplitz form; thus the potentials may each be evaluated using a single fast matrix-vector product with the FFT. Section IIIB discusses our model for the time-harmonic bowl-shaped transducer. Section IV presents a validation of our approach by comparing to simulations performed with the HITU Simulator MATLAB toolbox (Soneson, Accessed: 2020-05-06, 2017). In Section V we perform convergence tests for each of the harmonics for a range of problem setups. We present our findings on the rates of convergence of the approximation as the domain is increased and present a rule of thumbs for designing the meshes to ensure each harmonic is accurately approximated. In Section VI we present how the hierarchy of meshes is used in practice with our volume potential approach, including the interpolation of approximations between the meshes. Here we present some performance details for this three-dimension full-wave approach on a single workstation. Finally, in Section VIII we present our conclusions and discuss the relevance of this work to other numerical techniques for FUS.

## II. NONLINEAR ACOUSTICS IN THE FREQUENCY DOMAIN

Acoustic fields produced by FUS transducers are commonly modelled by the Westervelt equation (Hamilton *et al.*, 1998):

$$\nabla^2 p - \frac{1}{c_0^2} \frac{\partial^2 p}{\partial t^2} - \frac{2\alpha_0}{c_0^{1-\eta}} \frac{\partial}{\partial t} (-\nabla^2)^{\eta/2} p = -\frac{\beta}{\rho_0 c_0^4} \frac{\partial^2 p^2}{\partial t^2}, \quad (1)$$

where  $p$  is the acoustic pressure,  $c_0$  is the speed of sound,  $\rho_0$  is the medium density,  $\beta$  the non-linearity parameter, and  $\alpha_0$  and  $\eta$  are medium specific attenuation parameters. The fractional Laplacian appearing in (1) was first introduced in (Chen and Holm, 2004) in order to incorporate frequency dependent power law attenuation. More specifically, in the frequency domain, it generates a complex wavenumber of the form

$$k = \frac{\omega}{c_0} + i\alpha; \quad \alpha = \alpha_0 |\omega|^\eta, \quad (2)$$

for  $\alpha_0 |\omega|^{\eta-1} c_0 < 0.1$  (Szabo, 1994), where  $\omega$  is the angular frequency of the transducer. The power law exponent is typically in the range  $1 \leq \eta \leq 2$ . We note that this power law attenuation can also be incorporated via a temporal convolution, as was originally proposed in (Szabo, 1994); we refer the reader to (Treeby and Cox, 2010) for a review of power law attenuation techniques.

In this article, we assume that the operation time of the transducer is long when compared to the period of the signal. Therefore, the total acoustic pressure can be written as the following sum over harmonics (as in (Du and Jensen, 2013; Soneson, 2017)):

$$p(\mathbf{x}, t) = \text{Re} \left\{ \sum_{n=1}^{\infty} p_n(\mathbf{x}) e^{-in\omega t} \right\}, \quad (3)$$



where  $*$  denotes complex conjugation. Many numerical schemes in the literature consider the time-harmonic form (3), e.g., (Campos-Pozuelo *et al.*, 1999; Du and Jensen, 2013; Sonesson, 2017; van 't Wout *et al.*, 2015), likely owing to the distinct advantages of a frequency domain approach:

- the challenging task of choosing/developing an efficient time stepping scheme can be avoided;
- arbitrary frequency-dependent attenuation power laws can be easily incorporated (whereas in the time domain one has to contend with the fractional Laplacian);
- methods such as the boundary element method and volume integral equation method, can be applied directly;
- the computation regions for higher harmonics can be reduced, thereby making simulations more efficient.

It is this final point that we study in this article.

The form (3) is not well suited for substitution into (1) since the right-hand of (1) requires the computation of a product. For such a product, expressions in which real or imaginary parts are required to be taken lead to cumbersome algebra. Therefore, it is more straightforward to use the following expression, which is equivalent to (3):

$$p(\mathbf{x}, t) = \frac{1}{2} \sum_{n=1}^{\infty} (p_n(\mathbf{x})e^{-in\omega t} + p_n^*(\mathbf{x})e^{in\omega t}). \quad (4)$$

Substituting (4) into (1) and matching coefficients of  $e^{-in\omega t}$  for  $n \geq 1$  yields

$$\nabla^2 p_n + k_n^2 p_n = \frac{\beta\omega^2}{2\rho_0 c_0^4} n^2 \sum_{m=1}^{\infty} p_m (p_{n-m} + 2p_{m-n}^*), \quad (5)$$

for  $n = 1, 2, \dots$ , where  $p_n = 0$  for  $n \leq 0$ , and the complex wavenumbers are defined as

$$k_n = \frac{n\omega}{c_0} + i\alpha(n\omega). \quad (6)$$

The equations (5) can be further simplified by neglecting small terms on the right-hand side, which is appropriate in the weakly nonlinear case, as was considered in, e.g., (Du and Jensen, 2013). Specifically, we neglect all terms  $p_i p_j$  and  $p_i p_j^*$  for which  $i + j > n$ , for  $n = 1, 2, \dots$ , thus giving

$$\nabla^2 p_n + k_n^2 p_n = \frac{\beta \omega^2}{2\rho_0 c_0^4} n^2 \sum_{m=1}^{n-1} p_m p_{n-m}. \quad (7)$$

This is a cascade of inhomogeneous Helmholtz equations in which each right-hand side is a combination of products of lower harmonics. Therefore, we can solve the equations sequentially, starting from  $n = 1$ .

We note that the assumption of weak nonlinearity is valid for a wide range of FUS applications for thermal ablation. However, for extremely high focal pressures such as those sometimes encountered in lithotripsy, where pressures much higher than 20MPa can be seen, the terms neglected above become significant (Izadifar *et al.*, 2017). Therefore, a modified approach would be required, however we do not consider this case here.

### III. VOLUME POTENTIALS

The equations (7) are each of the general form

$$\nabla^2 u + k^2 u = f(\mathbf{x}), \quad \mathbf{x} \in \mathbb{R}^3. \quad (8)$$

176 Via Green's theorem (see, e.g., (Colton and Kress, 2013; Costabel, 2015)) it can be seen  
 177 that the following volume potential satisfies (8):

$$u(\mathbf{x}) = - \int_{\mathbb{R}^3} G_k(\mathbf{x}, \mathbf{y}) f(\mathbf{y}) d\mathbf{y}, \quad \mathbf{x} \in \mathbb{R}^3, \quad (9)$$

178 where  $G_k$  is the fundamental solution to the Helmholtz equation, also known as Green's  
 179 function:

$$G_k(\mathbf{x}, \mathbf{y}) = \frac{e^{ik|\mathbf{x}-\mathbf{y}|}}{4\pi|\mathbf{x}-\mathbf{y}|}, \quad \mathbf{x} \neq \mathbf{y}. \quad (10)$$

180 This function is singular when  $\mathbf{x} = \mathbf{y}$ , however integrals of the function across this sin-  
 181 gularity may be evaluated using principal value techniques or appropriate coordinate  
 182 transformations, as we shall see in Section III A. We note that the integral in (9) is over an  
 183 infinite domain, however in practice we replace this with a finite domain of integration,  $D$ .  
 184 So we have that

$$u(\mathbf{x}) = - \int_D G_k(\mathbf{x}, \mathbf{y}) f(\mathbf{y}) d\mathbf{y} + \varepsilon(D), \quad \mathbf{x} \in D \subset \mathbb{R}^3, \quad (11)$$

185 where  $\varepsilon(D)$  an error incurred by the introduction of a finite integration domain. Since the  
 186 FUS field is highly focused, a sensibly chosen finite  $D$  will yield a negligibly small error. It  
 187 is the purpose of this article to investigate how small  $D$  can be made whilst still yielding  
 188 accurate approximations to  $u$ .

For clarity, we write out this integral representation (11) for each of the first five harmonics:

$$p_2(\mathbf{x}) = -\frac{2\beta\omega^2}{\rho_0 c_0^4} \int_{D_2} G_{k_2}(\mathbf{x}, \mathbf{y}) p_1^2(\mathbf{y}) d\mathbf{y}, \quad (12)$$

$$p_3(\mathbf{x}) = -\frac{9\beta\omega^2}{\rho_0 c_0^4} \int_{D_3} G_{k_3}(\mathbf{x}, \mathbf{y}) p_1(\mathbf{y}) p_2(\mathbf{y}) d\mathbf{y}, \quad (13)$$

$$p_4(\mathbf{x}) = -\frac{8\beta\omega^2}{\rho_0 c_0^4} \int_{D_4} G_{k_4}(\mathbf{x}, \mathbf{y}) (p_2^2(\mathbf{y})$$

$$+ 2p_1(\mathbf{y})p_3(\mathbf{y})) d\mathbf{y}, \quad (15)$$

$$p_5(\mathbf{x}) = -\frac{25\beta\omega^2}{\rho_0 c_0^4} \int_{D_5} G_{k_5}(\mathbf{x}, \mathbf{y}) (p_1(\mathbf{y})p_4(\mathbf{y})$$

$$+ p_2(\mathbf{y})p_3(\mathbf{y})) d\mathbf{y}, \quad (16)$$

where we have introduced the domains  $D_i$ ,  $i = 2, 3, \dots$ , appropriate sizes of which are to be determined. In a homogeneous medium, the first harmonic  $p_1$  is merely the incident field generated by the transducer, which we can compute anywhere in  $\mathbb{R}^3$ , as is discussed in Section III B. Note finally that the Green's functions in each of (12)–(16) possess the appropriate wavenumber for that harmonic,  $k_n$ , for  $n = 2, 3, 4, 5$ .

#### A. Efficient computation of the volume potential

FUS problems are renowned for their challenging high-frequency nature, with domain sizes up to hundreds of wavelengths in each of the three dimensions. Therefore, the (singular) integrals in (12)–(16) are potentially enormously expensive to approximate.

We choose the integration domains  $D_i$  to be cuboidal in shape and to be discretized into uniform voxel grids  $\mathcal{V}(D_i)$  so that the discrete form of the integral operator becomes

200 a Toeplitz matrix. A Toeplitz matrix of dimension  $N$  has the property that it may be  
 201 embedded in a circulant matrix of dimension  $2N$ , with which a matrix-vector product can  
 202 be computed with  $\mathcal{O}(2N \log 2N)$  complexity using the fast-Fourier transform (FFT); see,  
 203 e.g., (Groth *et al.*, 2020) for more details.

For the voxels in which the Green’s function’s singularity is located, we approximate the  
 integral by the integral over a sphere of radius  $a$ , chosen such that the sphere’s volume is  
 equal to that of the voxel. This integral can then be transformed into spherical coordinates,  
 which is convenient because the Jacobian determinant of the transformation cancels the  
 singularity in the Green’s function. In the non-singular voxels we approximate the volume  
 potential integral by the midpoint rule. This gives us the simple quadrature rule

$$\begin{aligned} & \int_{V_j} G(\mathbf{x}_i, \mathbf{y}) f(\mathbf{y}) d\mathbf{y} \\ &= \begin{cases} \frac{1}{k^2} \{e^{ika}(1 - ika) - 1\} f(x_j), & \mathbf{x}_i \in V_j, \\ (\delta x)^3 G(\mathbf{x}_i, \mathbf{x}_j) f(\mathbf{x}_j), & \mathbf{x}_i \notin V_j, \end{cases} \end{aligned} \quad (17)$$

204 for  $i, j = 1, \dots, N$ , where  $N$  is the number of voxels in the grid and  $\delta x$  is the side length  
 205 of each voxel  $V_j$ . This is reminiscent of the ‘discrete dipole approximation’ often used in  
 206 electromagnetic scattering calculations (Draine and Flatau, 1994). One can choose to opt  
 207 for a more sophisticated quadrature rule here, however, this simple approach suffices for our  
 208 purposes.

## B. **FUS** incident field

In a homogeneous medium there is no scattering and therefore the first harmonic,  $p_1$ , can be obtained directly from an appropriate model of the time-harmonic field generated by the **FUS** source. In this paper, we consider bowl-shaped ultrasound transducers, which are designed to focus acoustic energy at a prescribed location, typically the centre of curvature of the bowl. More specifically, we consider for simplicity a single-element bowl-shaped transducer and discretise the surface using a Rayleigh integral type approach described below. We note that we are not exploiting symmetries in our approach and therefore more sophisticated multi-element transducer arrays, such as those in (Gavrilov and Hand, 2000; G  lat *et al.*, 2011; Kreider *et al.*, 2013), can be incorporated in a straightforward manner.

To discretise the surface of the bowl transducer, we use evenly spaced points following (Deserno, 2004). At each of the evenly spaced point we place a monopole source, the expression for which is given by (10). Summing over the monopole sources gives the (unnormalised) first harmonic at any  $\mathbf{x} \in \mathbb{R}^3$  as

$$\tilde{p}(\mathbf{x}) = \frac{A}{n_p} \sum_{i=1}^{n_p} G_k(\mathbf{x}, \mathbf{r}_i), \quad (18)$$

where  $n_p$  is the number of points,  $\mathbf{r}_i$  are their locations on the bowl, and  $A$  is the total surface area of the bowl.

We note that in (18) no amplitude has been specified for the monopole sources. We instead choose to normalise the field to produce a prescribed total radiated power,  $\Pi$ , which is obtained by integrating the intensity over a sphere surrounding the source (Kinsler *et al.*, 1999). For a bowl-shaped transducer, the field is directed, so rather than integrating over a

229 sphere, it suffices to integrate over a disc covering the open end of the bowl. This can be  
 230 written as

$$\Pi(p) = \frac{1}{2\rho_0 c_0} \int_0^{2\pi} \int_0^R p^2(r, \theta) dr d\theta, \quad (19)$$

231 where  $R$  is the outer radius of the bowl. Thus, the normalised first harmonic to yield a  
 232 prescribed radiated power  $\Pi_0$  is given as

$$p_1(\mathbf{x}) = \sqrt{\frac{\Pi_0}{\Pi(\tilde{p})}} \tilde{p}. \quad (20)$$

233 In our experiments, we take  $n_p = 4096$ , which equates to approximately ten monopole  
 234 sources per fundamental wavelength. Such a large value was required to avoid undesired  
 235 interference patterns between the bowl and focus.

236 The two bowl transducer geometries considered in this article are taken from the Sonic  
 237 Concepts website ([Sonic Concepts](#), [Accessed: 2020-08-19](#)) and are detailed in Tab. I. Two

	$f_0$ (MHz)	$l$ (mm)	$R$ (mm)
H101	1.1	63.2	32
H131	1.1	35	16.5

TABLE I. Operating frequencies and geometrical parameters of bowl transducers considered, taken from ([Sonic Concepts](#), [Accessed: 2020-08-19](#)). The geometrical parameters are the geometric focal length  $l$  and the outer radius  $R$ . These can also be seen depicted in Fig. 1.

238

239

240 propagation media are considered throughout: water and liver. The acoustic parameters for  
 242 these are detailed in Tab. II.

	$\rho_0$ (kg/m <sup>3</sup> )	$c$ (m/s)	$\beta$	$\alpha_0$	$\eta$ (dB/m)
Water	1000	1480	3.5	0.2	2
Liver	1060	1590	4.4	90.0	1.1
Kidney	1050	1570	4.7	10	1

TABLE II. Relevant medium parameters for water, liver and kidney at 1MHz ([Azhari, 2010](#); [Duck, 2013](#)). The parameters  $\alpha_0$  and  $\eta$  pertain to the absorption power law in (2).

### C. How many points per wavelength?

Before deploying our scheme to compute high-order harmonics, it is necessary to understand the convergence rate as the mesh is refined, thereby enabling an adequate resolution to be chosen for later investigations. In this article, we focus on achieving approximations with relative  $L^2$  errors close to 1%.

To determine the convergence rate, we consider computing the second harmonic generated by the H131 transducer in liver, using equation (12). The configuration of the transducer is shown in Fig. 2; the bowl transducer is located at the origin and is directed along the  $x$ -axis. For the integration domain  $D_2$  in (12) we take the white box in Fig. 2. This box is illustrated with detailed dimension definitions in Fig. 1. The domain  $D_2$  is defined as

$$D_2 = [l - L, l + d] \times [-R, R] \times [-R, R], \quad (21)$$

where  $d$  is the distance of interest beyond the focus,  $l$  is the geometric focal length, and  $R$  the outer radius (see Fig. 1). The length  $L$  is defined as  $L = \sqrt{l^2 - R^2} - \epsilon$  with  $\epsilon$  chosen as a small displacement from the bowl in order to avoid the possibility of  $\mathbf{x} = \mathbf{r}_i$  in (18), for



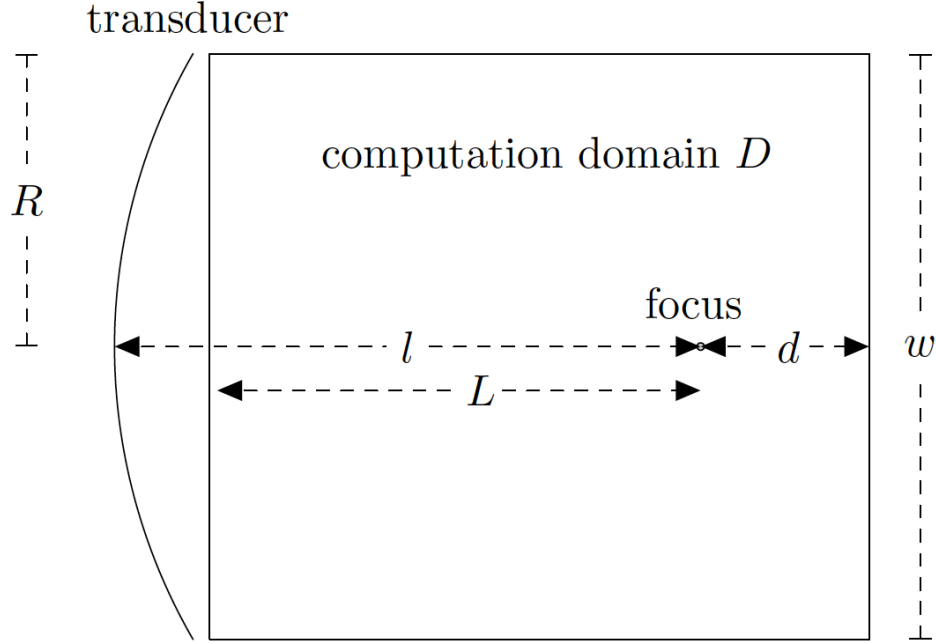


FIG. 1. Description of a generic computation domain  $D$  with length  $L + d$  and width (and depth)

$w$ .

which the monopole sources are undefined; we take  $\epsilon = 0.1\text{mm}$ . In this article, we suppose that the region near the focus is of primary interest, therefore from a computational point of view, we desire to shrink the computation domain to be much shorter and narrower than  $L$  and  $w$ , i.e., more localised around the focus, in order to reduce computational load. The extent to which this shrinking can be done without losing accuracy is the focus of sections V-VI. The values of  $L$  and  $w$  defined above represent our default computation domain. The value the distance  $d$  depends on the user's interest in the region beyond the focus. In the absence of scatterers beyond the focus, the field in this region after the focus will not affect the intensity at the focus. In the present example, the total radiated power of the transducer is set as  $\Pi_0 = 100\text{W}$  and the operating frequency is  $f_0 = 1.1\text{MHz}$ .

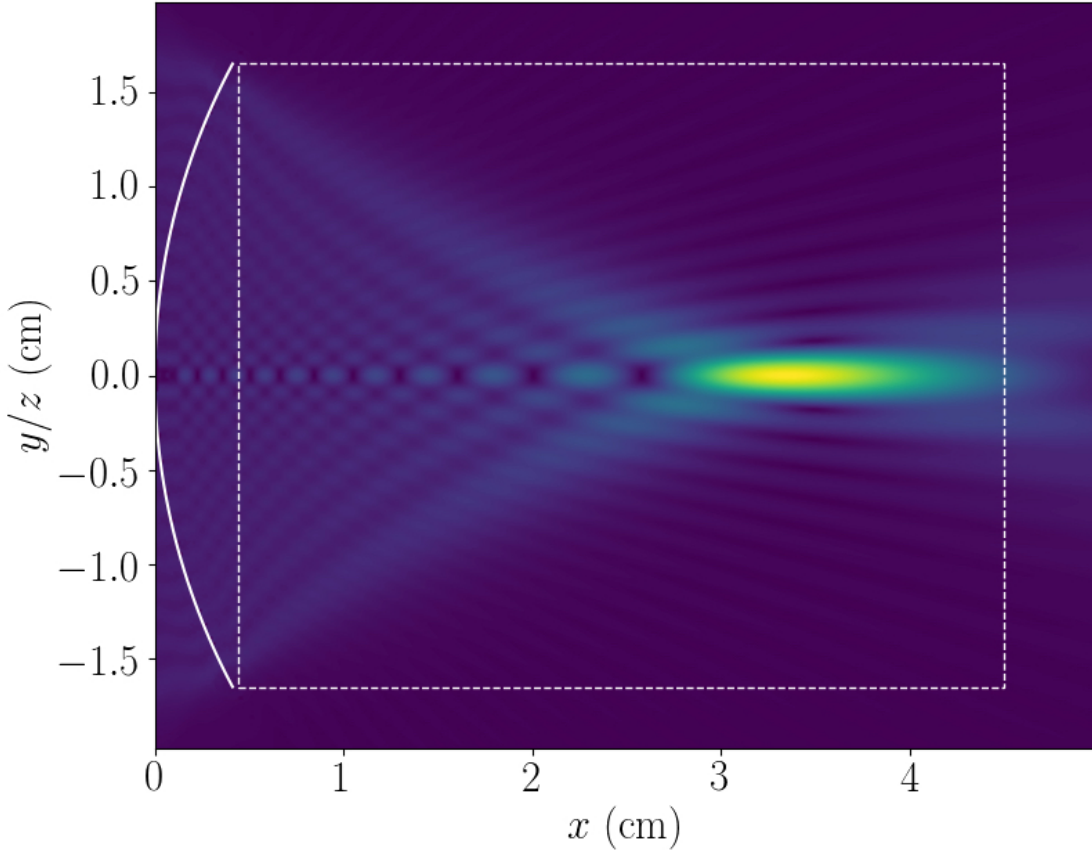


FIG. 2. Magnitude of the first harmonic generated by the H131 transducer in liver. The bowl transducer is represented by the arc at the far left. The dashed white line outlines the computation domain  $D_2$  used to compute the second harmonic shown in Fig. 4.

268 The volume potential in (12) is computed using the method outlined in Section III A  
 269 with increasingly refined voxel meshes. Specifically, we build meshes with voxel dimension  
 270  $\delta x = \lambda/(2n_w)$ , where  $\lambda = c/f_0$  is the fundamental wavelength and  $n_w$  is the ‘number of  
 271 voxels per wavelength’. The factor 2 in the denominator is to account for the fact that  
 272 we are computing a field with wavelength  $\lambda/2$ , i.e., the second harmonic. The values of  $n_w$   
 273 considered are from 4 to 20, and a reference solution, denoted  $p_2^r$ , is computed using  $n_w = 35$ .

For each value of  $n_w$ , the relative  $L^2$ -error of the field  $p_2$  along the  $x$ -axis is computed; this is defined as

$$\text{Error} = \frac{\|p_2 - p_2^r\|}{\|p_2^r\|} \times 100\%, \quad (22)$$

where  $\|\cdot\|$  denotes the  $L^2$ -norm along the  $x$ -axis, i.e.,

$$\|p_2\| := \left( \int_{l-L}^{l+d} |p_2(x)|^2 dx \right)^{1/2}. \quad (23)$$

We approximate the integrals in (22) using the midpoint rule with the mesh nodes of the reference solution,  $p_2^r$ , being used as the quadrature nodes.

The convergence results are shown in Figure 3. As is to be expected from the midpoint rule, quadratic convergence is obtained. From the graph we can read off that an error smaller than 1% is achieved with  $n_w > 5$ . Therefore we choose to take  $n_w = 6$  for all harmonics in the experiments in the remainder of the article. The approximation to the second harmonic with  $n_w = 6$  is shown in Fig. 4 and can be seen to be indistinguishable from the reference solution.

#### IV. VALIDATION OF NUMERICAL SCHEME

To validate our approach for the computation of higher harmonics via the evaluation of the volume potentials in (12)-(16), we present a qualitative comparison to approximations obtained using *HITU Simulator* (Soneson, Accessed: 2020-05-06). HITU simulator is an open-source MATLAB implementation of the high-order parabolic approximation to the axisymmetric Westervelt equation, i.e., the wide-angle Khokhlov-Zabolotkaya-Kuznetsov (WAKZK) equation. The method is detailed by the author of HITU simulator in (Soneson,

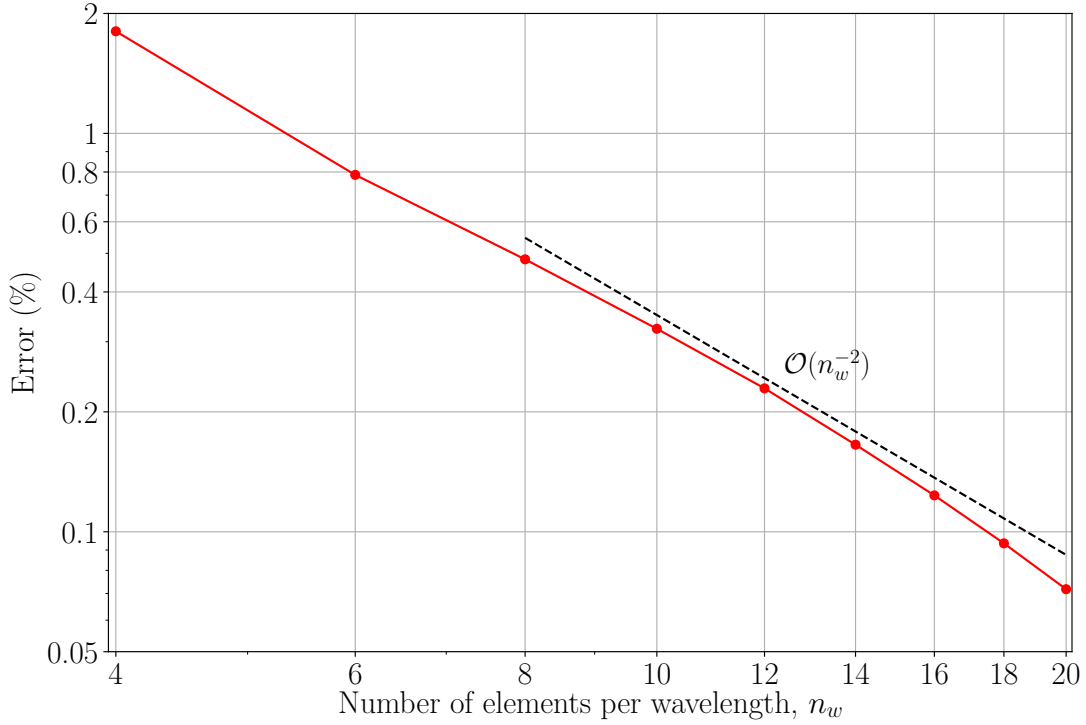


FIG. 3. The convergence of the quadrature rule for the computation of the second harmonic via (12). The convergence rate is quadratic in  $n_w$  and an error of smaller than 1% is achieved with  $n_w > 5$ .

(2017). The assumption of axisymmetry allows the dimension of the problem to be reduced by one and hence facilitates rapid simulations.

We consider two configurations:

1. H131 transducer at output power 50W in water;
2. H101 transducer at output power 100W in liver.

The first five harmonics along the  $x$ -axis are shown in Fig. 5 and Fig. 6. In both cases we observe good qualitative agreement with the approximations obtained using HITU simulator

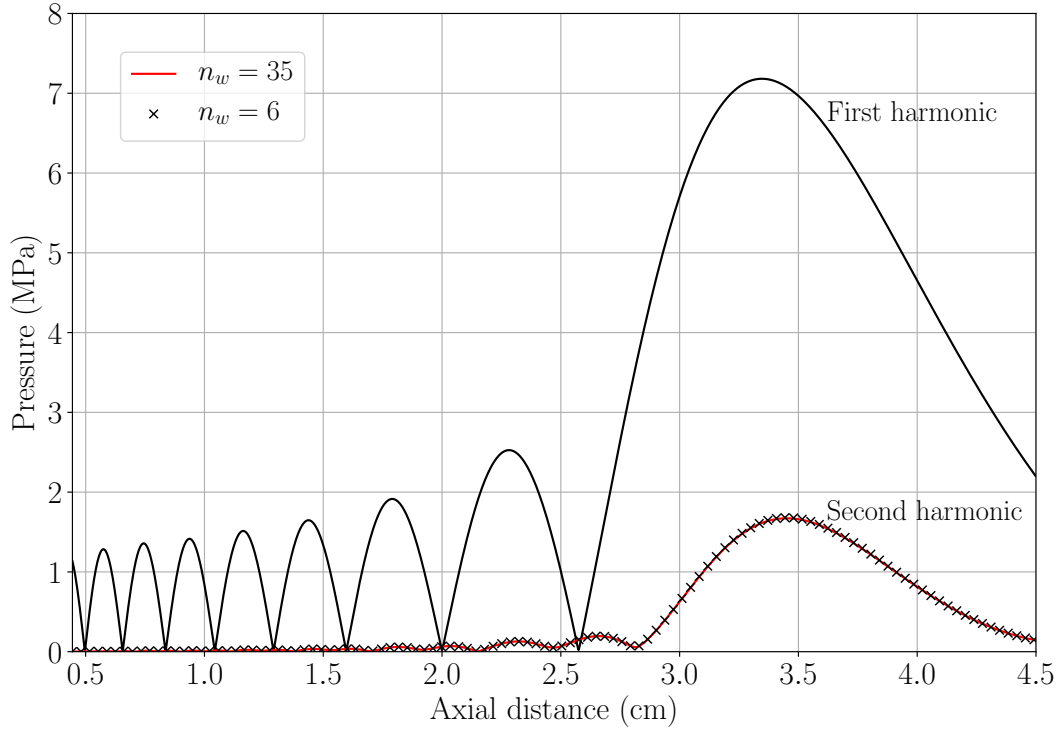


FIG. 4. The first and second harmonics along the  $x$ -axis for the H131 transducer in liver. With 6 voxels per wavelength the approximation to the second harmonic is indistinguishable from the reference solution.

in the region around the focus, whereas towards the transducer the two methods disagree. This is due to the parabolic assumption made in the derivation of the WAKZK equation, which is only accurate when sufficiently far from the transducer. The volume potential method on the other hand approximates solutions to the Westervelt equation so can be taken to be accurate in this ‘near field’ region. Indeed, the computation of the first harmonic in our approach, as outlined in Section III B, is equivalent to a Rayleigh integral method.

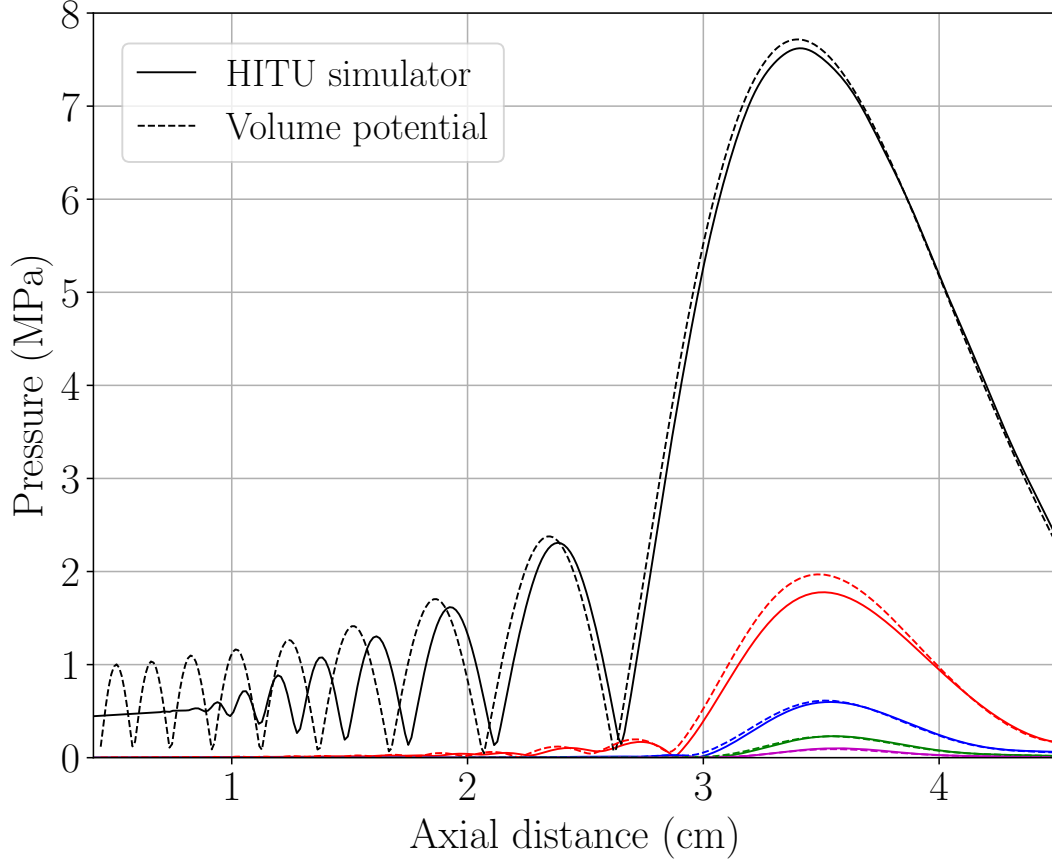


FIG. 5. Comparison of the VIE approach with HITU simulator for the first five harmonics generated by the H131 transducer operating at a power of 50W in water.

We observe that the volume potential method predicts a slightly larger amplitude for the first and second harmonics than HITU simulator, which may be because the energy flow of the higher harmonics to lower harmonics is neglected in the derivation of (7). However, the agreement for the third, fourth and fifth harmonics is almost perfect. The two examples considered have considerably different attenuation power law parameters, thus the strong agreement with HITU simulator for both examples demonstrates that the attenuation is being handled correctly in the volume potential method.

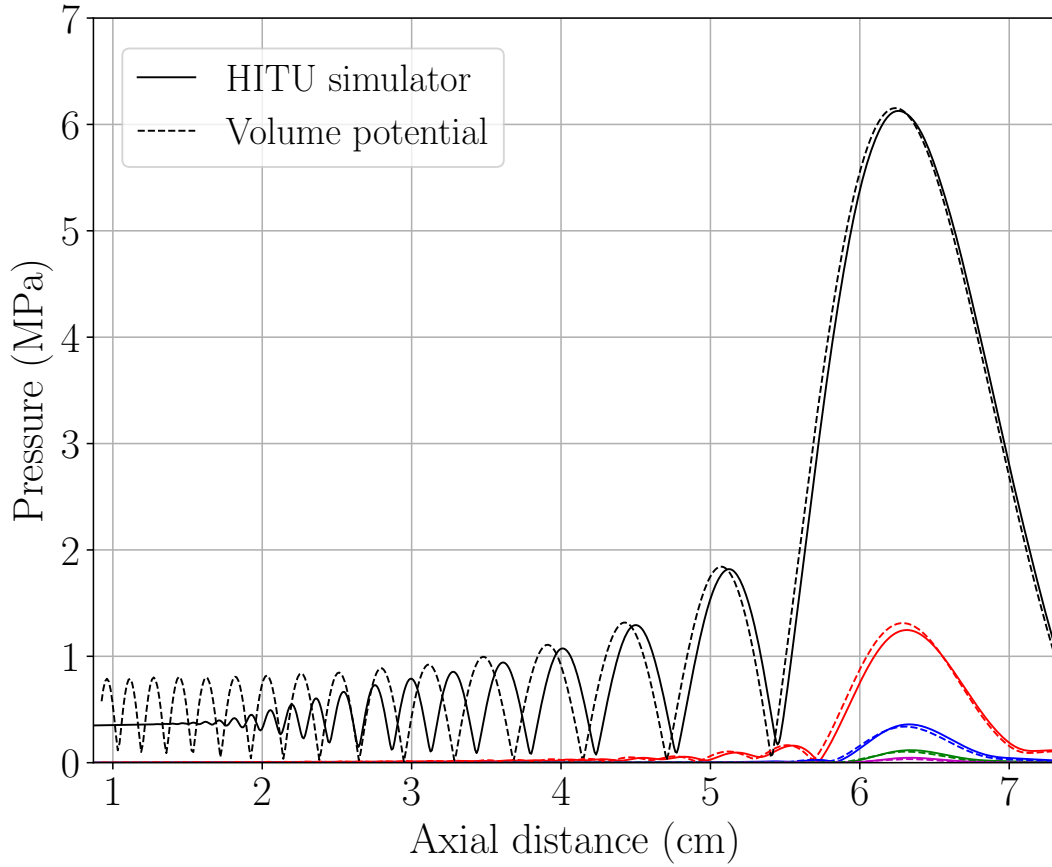


FIG. 6. Comparison of the VIE approach with HITU simulator for the first five harmonics. H101 transducer at power 100W in liver.

## V. COMPUTATION DOMAINS FOR SUCCESSIVE HARMONICS

In this section we aim to determine the amount by which we can restrict the computation domain while retaining accurate approximations, and thus enable acceleration of our simulations.

The main region of interest to practitioners is that around the focus, since this is where tissue ablation occurs. Ideally one would compute only on that small region. This, however,

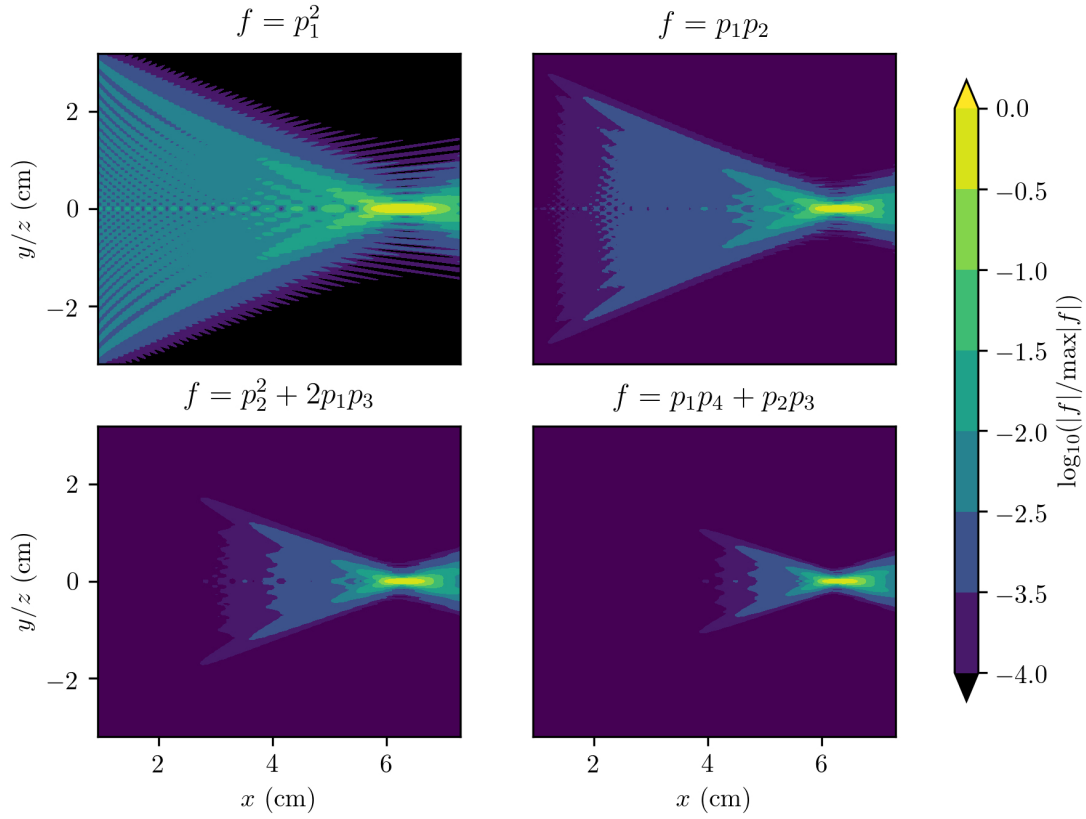


FIG. 7. The relative magnitudes of the right-hand side functions  $f$  as described in equation (24) for the H101 transducer in liver, at 100W. These plots show how the function to be convolved with the Green's function becomes more localised as the harmonics increase.

leads to the second harmonic (and thus also the third, fourth, etc.) being poorly approx-  
 imated since these harmonics are generated by the accumulation of acoustic energy over  
 distance. So we seek a balance between accuracy and computational cost. Here we shall  
 aim to keep the error in each harmonic below 1% (relative to the magnitude of the first  
 harmonic) whilst shrinking the integration regions  $D_i$  in (12)-(16) as much as possible.

It is important to note that (in this homogeneous setting), the field beyond the focal point  
 has no influence on the field in front of it, i.e., the waves propagate only in the positive  $x$ -



direction. This means that our exploration of domain shrinking only applies to the region between the transducer and the focal point. Beyond the focus we keep the domain length in the  $x$ -direction fixed. In most **FUS** settings, the practioners are not interested in the field far beyond the focal region, therefore the inability to shrink the region beyond the focus does not greatly affect the gains achieved from shrinking the computational domain before the focus.

Each of the equations (12)-(16) has the form

$$p(\mathbf{x}) = C \int_D G_k(\mathbf{x}, \mathbf{y}) f(\mathbf{y}) d\mathbf{y}, \quad (24)$$

where  $f = p_1^2, p_1 p_2, \dots$ ,  $C$  is the appropriate constant, and  $k$  is the appropriate wavenumber. In order to accurately approximate  $p$ , the integration domain  $D$  must enclose the region where the integrand is non-negligible. Outside of this region, we can discard the contributions. The magnitude of the integrand is dictated by the function  $f$ , which has the units of intensity. In order to have an idea of how localised the different functions  $f$  are, we plot them for a particular example in Fig. 7. The setup considered in the figure is the H101 transducer at 100W in liver. The figure shows the magnitudes of  $f$  scaled by their maximum values (at the focus) and converted to a log-scale. Consider the top-left image: this is the  $f$  required for the computation of the second harmonic. We can see that the magnitude is significant all the way back to the transducer, implying that we must include all this area in the integration domain  $D$ . For the remaining images, corresponding to the third, fourth and fifth harmonics, the functions become increasingly more localised in both the  $x$  and  $y/z$  dimensions, suggesting that the required integration domain can be considerably smaller than that for the second harmonic.

To investigate this more rigorously, we perform convergence tests for each harmonic as the relevant integration domain  $D$  is restricted. That is, we take the harmonics generated on the domain in (21) as the reference solutions  $p_l^r$ ,  $l = 2, 3, 4, 5$ , and then compute the same harmonics on successively smaller domains and compare the approximations to the reference. The error of an approximation  $p_l$  is computed along the  $x$ -axis as

$$\text{Error} = \frac{\|p_l - p_l^r\|}{\|p_1^r\|} \times 100\%. \quad (25)$$

Note that the harmonic field in the denominator is that of the first harmonic. This is done so that the error function incorporates the diminishing size of successive harmonics. For example, if the fifth harmonic is negligibly small relative to the first harmonic (and so not worth calculating), the error will reflect this by being very small.

As a measure of the “localisedness” of the functions  $f$ , we use the quantity plotted in Fig. 7, which we denote as  $Q$ :

$$Q(\mathbf{x}) := \log_{10} \left( \frac{|f(\mathbf{x})|}{\max |f(\mathbf{x})|} \right). \quad (26)$$

In the convergence tests, the integration domain is chosen as the smallest cuboidal domain  $D$  such  $Q(\mathbf{x}) < Q_0$  for  $\mathbf{x} \in D$ , where  $Q_0$  is a given threshold.

The first configuration we test is the H131 transducer in water at an output power of 100W. The convergence for each harmonic is shown in Fig. 8. We notice that the convergence of the second harmonic drops suddenly once the error dips below 1% – this is because the computation domain is close to the size of the reference domain by this point. This is illustrated more clearly in Fig. 9 where the same data as in Fig. 8 is shown but now plotted against the size of the computation domain as a fraction of the reference domain, rather

than against  $Q_0$ . By ‘fraction’ of the domain, we mean the scaling factor such that the length  $L'$  and width  $w'$  of the shrunk domain are given by

$$L' = \text{fraction} \times L, \quad w' = \text{fraction} \times w.$$

370

Fig. 9 shows that, to achieve less than 1% error in  $p_2$ , the computation domain must extend all the way to the transducer. For the higher harmonics, however, a different trend is

372

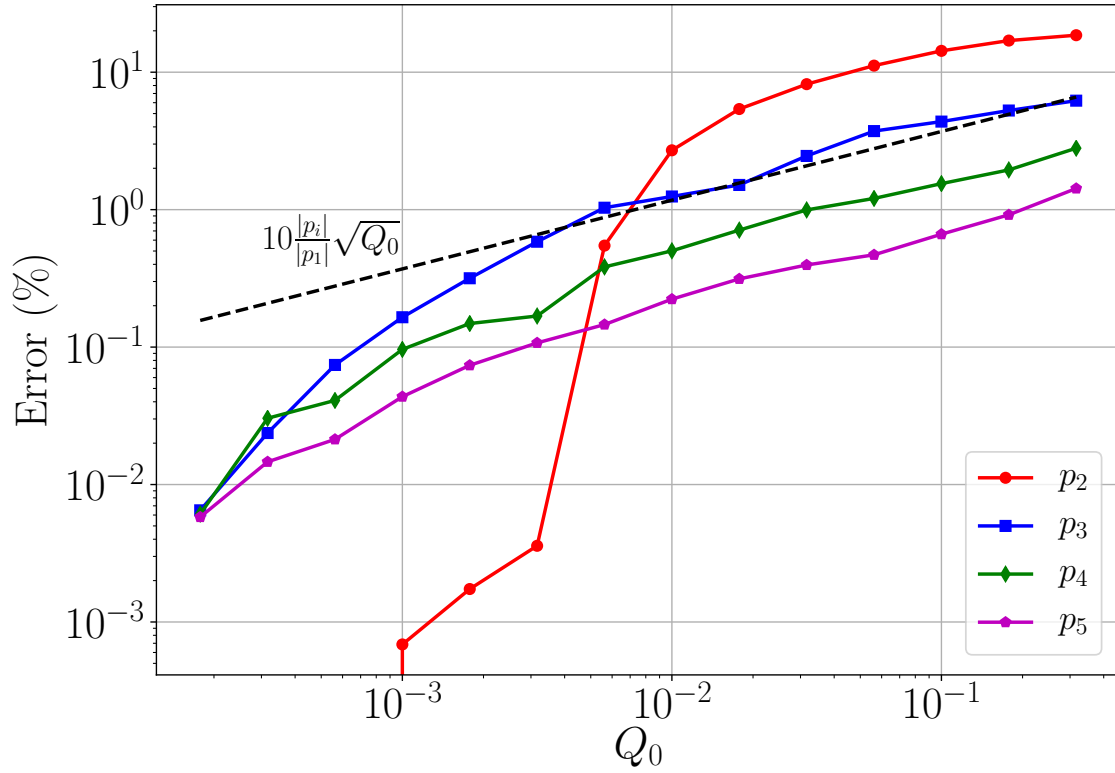


FIG. 8. Convergence of the approximations to harmonics  $p_i$ ,  $i = 2, \dots, 5$  as the domain of integration  $D_i$  for each is adjusted according to the function  $Q \geq Q_0$ , as defined in (26). The setup considered here is the H131 transducer at a power of 100W in water.

373

374

evident. In Fig. 8 we observe that the error curves for  $p_3, p_4, p_5$  each have the approximate behaviour

$$\text{Error}(p_i) \approx 10 \frac{\|p_i\|}{\|p_1\|} \sqrt{Q_0}, \quad i = 3, 4, 5, \quad (27)$$

where  $\|\cdot\|$  represents the  $L^2$ -norm. Although an interesting observation, the utility of the relationship (27) for dictating an appropriate computation domain for  $p_i$  is not immediately apparent, since it requires the computation of  $\|p_i\|$  before  $p_i$  has been computed. Determining an *a priori* approximation for  $\|p_i\|$  to make use of (27) would be a useful endeavour, however we do not undertake such a task in this article. Rather we seek to develop an approximate rule of thumb for choosing sensibly-sized computation domains for the harmonics. To this end, it is more straightforward to consider the convergence of the approximations in terms of physical distance, as is done in Fig. 9 and Tab. III.

By looking at the 1% error line in Fig. 9, it is possible to read off the size of the domains as fractions of the reference domain. The precise values are reported in Tab. III. A nested series of domains constructed according to this specification is shown in Fig. 10. Let us elaborate on the potential computational gain achieved using these nested domains compared to computing all harmonics on the reference domain.

The reference domain for the H131 transducer in water has dimensions [4.1cm, 3.3cm, 3.3cm] and is discretised into voxels of dimension  $\delta x = \lambda_5/6 \approx 45.1\mu\text{m}$ , i.e., fine enough to resolve the highest harmonic of interest. This mesh has  $901 \cdot 732 \cdot 732 \approx 4.8 \times 10^8$  voxels for the computation of all the harmonics. Using the nested domains built according to the specifications in Tab. III, we obtain a mesh for  $p_2$  with dimensions [4.1, 2.4, 2.4]cm, which is discretised into voxels of dimension  $\delta x = \lambda_2/6 \approx 113\mu\text{m}$ . This mesh has  $360 \cdot 211 \cdot 211 \approx 1.6 \times 10^7$  voxels,

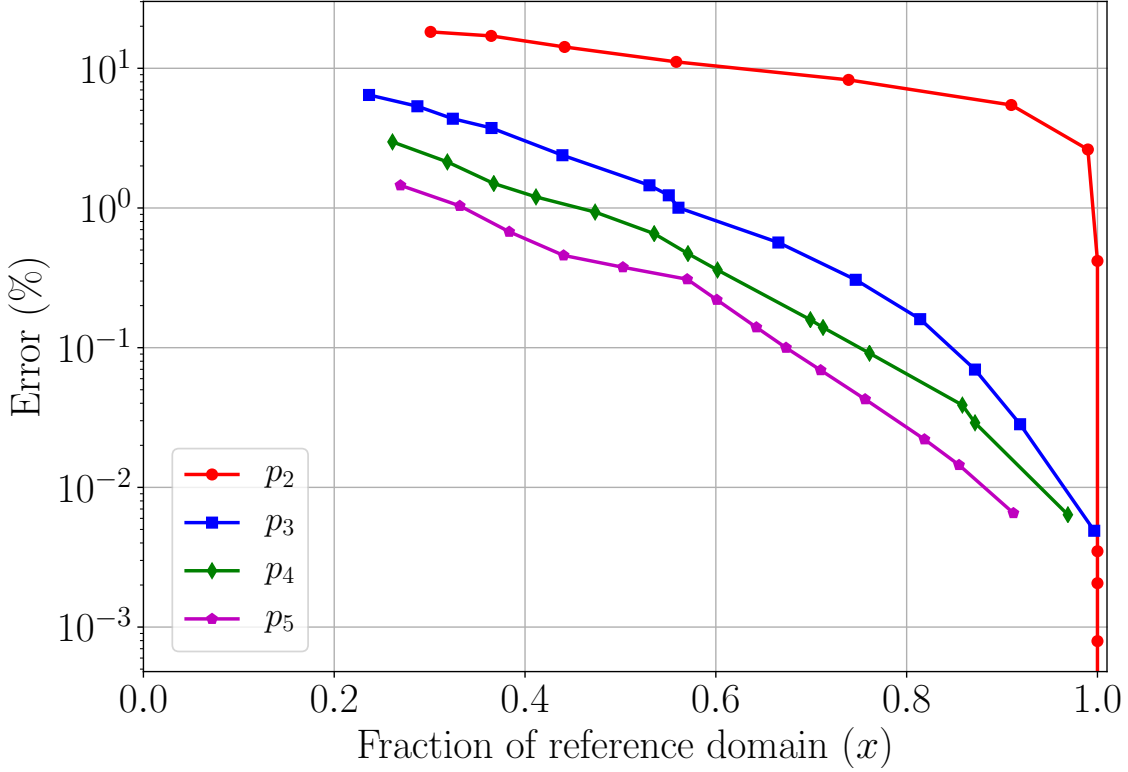


FIG. 9. Convergence for H131 transducer at 100W in water, as in Fig. 8, but now the error is plotted against the fraction of the total domain in the  $x$ -direction. This demonstrates that, to achieve an error smaller than 1%, the computation domains can be contracted significantly in the  $x$ -direction for harmonics higher than the second.

which is a factor of 30 smaller than the reference mesh. The meshes for the computation of  $p_3, p_4$  and  $p_5$  have  $1.22 \times 10^7$ ,  $6.1 \times 10^6$  and  $4.5 \times 10^6$  voxels, respectively. Thus the total number of voxels required for all harmonics is  $4 \times 4.8 \times 10^8 = 19 \times 10^8$  for the single mesh approach and  $3.9 \times 10^7$  for the nested meshing (summing over voxels in each of the four meshes). Hence we achieve close to a factor 50 reduction in computational load.

		$p_2$	$p_3$	$p_4$	$p_5$
H131 water	$x$	1	0.67	0.47	0.38
100W	$y/z$	0.74	0.39	0.20	0.13
H131 water	$x$	1	0.67	0.58	0.52
150W	$y/z$	0.71	0.40	0.39	0.21
H131 liver	$x$	1	0.56	0.25	0.26
100W	$y/z$	0.90	0.20	0.05	0.06
Rule of	$x$	1	0.75	0.65	0.61
thumb	$y/z$	1	0.67	0.5	0.4

TABLE III. Sizes of domains required to achieve less than 1% error for each harmonic as fractions of the reference domain (21). Since all domains are boxes, the fractions of the distances in the  $x$  and  $y/z$  directions are provided.

This improvement is impressive, however it is easily seen in Tab. III that this particular domain scaling does not apply to all transducer and material configurations. Therefore, we decide upon a simple rule of thumb for designing the separate computational domains that leads to domains greater than or equal to those given in Tab. III. Therefore, the errors incurred in using these domains will be even smaller than those obtained when using the ideal domains specified in the table.

A desirable rule for domain sizes would be the following:

Let  $[l + d, w, w]$  be the dimensions of domain  $D_2$  (see Fig. 1) for harmonic  $p_2$ ,  
 with corresponding wavelength  $\lambda_2$ . Then choose the dimensions of domain  $D_i$ ,  
 $i > 2$ , as  $[\frac{\lambda_i}{\lambda_2}l + d, \frac{\lambda_i}{\lambda_2}w, \frac{\lambda_i}{\lambda_2}w]$ . That is, the domain is scaled according to the  
 wavelength of the harmonic being considered.

With this rule for creating the domains, we observe that the number of voxels in each mesh  
 will almost be the same, save for a slight increase due to the fact that the distance  $d$  is not  
 being scaled. This amounts to a reduction in the overall number of DOF by a factor of  
 approximately  $(n/2)^3$  (in fact, slightly lower than this due to the unscaled portion of length  
 $d$ ), where  $n$  is the number of harmonics being computed.

In the next section, we outline an algorithm for evaluating the volume potentials over a  
 set of nested domains constructed according to the rule of thumb proposed above.

	N° voxels	Meshing	Interpolation	Evaluate $G_{k_i}$	Compute $p_i$
$p_2$	$1.86 \times 10^8$	26.1s	24m30s	4m54s	3m48s
$p_3$	$2.01 \times 10^8$	22.2s	3m9s	5m14s	4m9s
$p_4$	$2.15 \times 10^8$	23.9s	5m50s	5m27s	4m8s
$p_5$	$2.30 \times 10^8$	25.5s	7m12s	6m7s	7m5s

TABLE IV. Performance details for the volume potential approach on nested meshes with a resolution of six voxels per wavelength (for each harmonic). The configuration considered is the H101 transducer operating at 100W in water. Total time taken 1h23m11s.

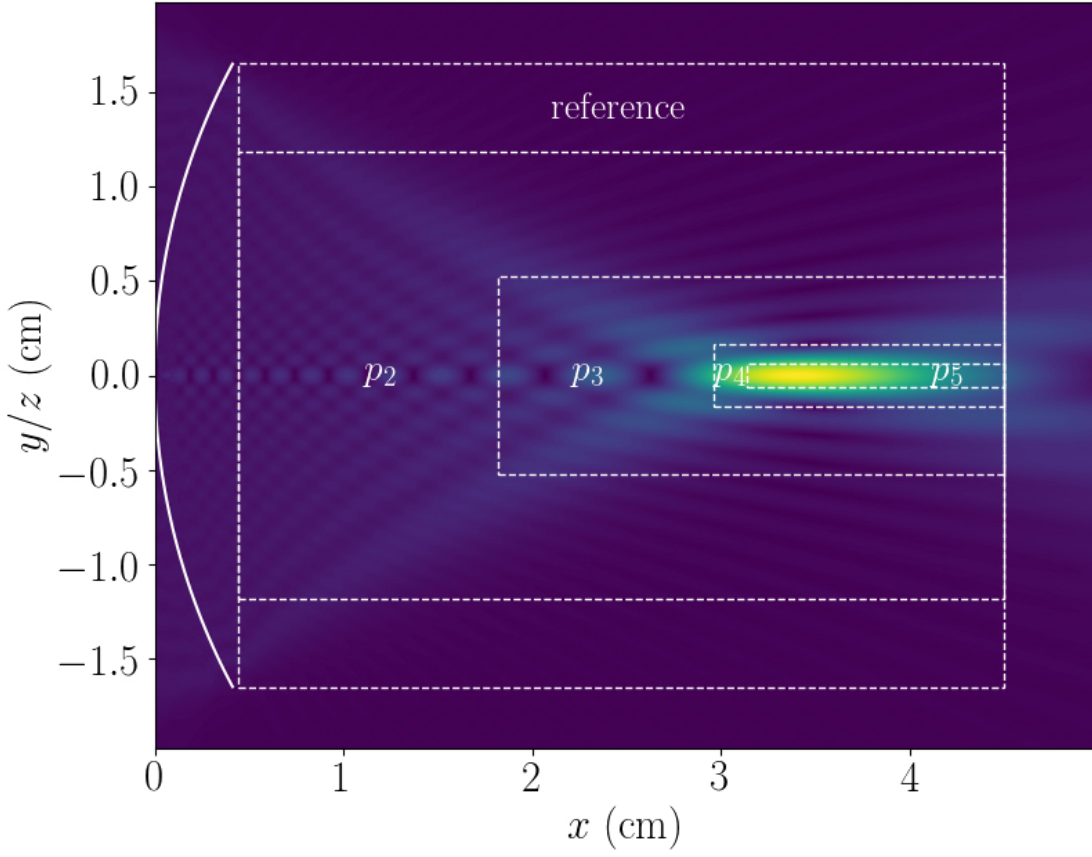


FIG. 10. Nested domains for the computation of successive harmonics while keeping relative error below 1%, for the H131 transducer operating at 100W in water. The domain used to compute the reference solution is in (21).

## VI. VOLUME POTENTIALS ON NESTED MESHES

To demonstrate the effectiveness of the volume potential evaluation on nested meshes, we present some final results detailing the computational performance of this approach. First we outline the algorithm for computing the first  $n$  harmonics:

**for**  $i = 2 \rightarrow n$  **do**



1. Create domain  $D_i$  for  $p_i$  and voxel mesh  $\mathcal{V}(D_i)$

2. Assemble components for integration (17):

(a) Evaluate/interpolate  $p_{i-1}, p_{i-2}, \dots, p_1$  at voxel centres in  $\mathcal{V}(D_i)$

(b) Evaluate integral of Green's function  $G_{k_i}$  over each voxel

3. Compute  $p_i$  via appropriate equation in (12)–(16)

**end for**

Note that in the above algorithm, for  $p_2$ , the pressure field  $p_1$  is evaluated over the voxel mesh  $\mathcal{V}(D_2)$  as described in Section III B. Whereas for later harmonics we perform interpolation of the earlier harmonics down onto the new mesh. In this work we have used linear interpolation, however if higher accuracy is required, we recommend quadratic interpolation (albeit at a higher computational cost). The second and third step each contain applications of the FFT: for the circulant embedding of the Green's function in step 2 (see, e.g., (Groth *et al.*, 2020)) and to perform the convolution required in the quadrature rule (17) in step 3. These FFTs are performed using the Python wrapper 'pyfftw' to the FFTW library (Frigo and Johnson, 2005).

As an example, we consider the H101 transducer operating at 100W in water run on a workstation with two sockets, each containing a 14-core Xeon E5-2690 v4 CPU, each supporting hyper-threading with two threads, and hence a total number of 56 threads. The total amount of RAM available on this machine is approximately 270GB, which is ample for the problems considered here. The first five harmonics along the  $x$ -axis are shown in Fig. 11, along with the approximation obtained with HITU simulator; again we see that the

volume potential approach predicts a larger peak in the second harmonic but in general a good qualitative agreement is observed.

To get a feel for the performance of our approach (of evaluating the volume potentials on nested meshes designed according to our proposed rule of thumb), the cost of each step in the above algorithm is detailed in Tab. IV. The largest mesh has 230 million voxels, as compared to 2.9 billion voxels without nested meshing. This represents a large saving, in both time and memory. The most expensive step reported in Tab. IV is the evaluation of the first harmonic  $p_1$  on  $\mathcal{V}(D_2)$ . This process was described in Section IIIB and has complexity  $\mathcal{O}(n_e N)$ , where  $n_e$  is number of points used to discretise the surface of the transducer and  $N$  is the number of voxels. Since we take  $n_e = 4096$ , this is a rather expensive procedure, even when parallelised over 56 threads. Therefore a transducer model using far fewer elements and/or a machine with more threads will lead to a large reduction in computation time for this step. Linear interpolation is computed efficiently using the `scipy` (Jones *et al.*, 2001–) `RegularGridInterpolator` command. The evaluation of  $G_{k_i}$  consists of a parallelised loop over the  $N$  voxels and then an FFT of a three-dimensional complex-valued array of size  $(2N_x, 2N_y, 2N_z)$ , where  $N_x, N_y, N_z$  are the number of voxels in each dimension. Then the computation of  $p_i$  consists of one forward and one inverse FFT of an array of size  $(2N_x, 2N_y, 2N_z)$ . The FFTs take advantage of multithreading, therefore can be easily accelerated through the use of more cores. Furthermore, it seems likely that optimising the FFT routine for the particular setting and using the FFTW C++ library directly will lead to further acceleration. Nevertheless, the current implementation yields fast and accurate predictions of the first five harmonics (in the cases considered).

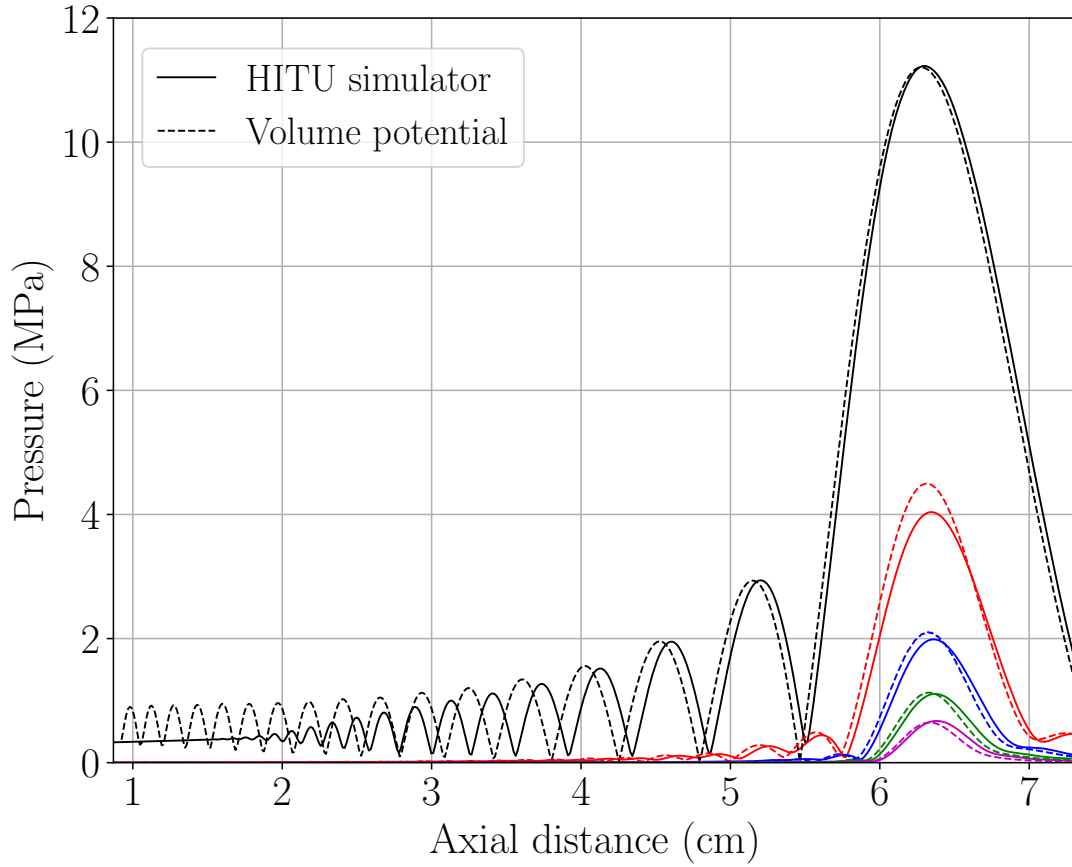


FIG. 11. The on-axis absolute pressure field for the first five harmonics generated by the H101 transducer at 100W in water, as computed using the volume potential approach on nested domains, designed to keep the relative error below 1%. The approximation obtained using the HITU simulator is provided for comparison.

## VII. EXTENSION TO INHOMOGENEOUS DOMAINS

We briefly consider the extension of this approach to the case of an inhomogeneous domain. That is, we suppose that the wavespeed,  $c(\mathbf{x})$ , and non-linearity parameter,  $\beta(\mathbf{x})$ , are now spatially varying. Further, we assume that the density is close to constant, i.e.,

472  $\rho(\mathbf{x}) \approx \rho_0$  (we comment on large density contrasts at the end of this section). The spatial  
 473 variation of  $c$  and  $\beta$  lead to backscattering of the field generated by the transducer, and thus,  
 474 rather than computing the harmonics via direct evaluation of volume potentials as before,  
 475 we must now in addition solve *volume integral equations* (VIEs) account for the scattering  
 476 effects.

Let the first harmonic of the *incident field* generated by the transducer be denoted as  $p^{\text{inc}}$ . Then VIEs for the first five harmonics are (see (Costabel, 2015)):

$$p_1(\mathbf{x}) - \int_{D_1} G_{k_1}(\mathbf{x}, \mathbf{y})(k_1^2(\mathbf{y}) - \bar{k}_1^2)p_1(\mathbf{y})d\mathbf{y} = p^{\text{inc}}(\mathbf{x}), \quad (28)$$

$$p_2(\mathbf{x}) - \int_{D_2} G_{k_2}(\mathbf{x}, \mathbf{y})(k_2^2(\mathbf{y}) - \bar{k}_2^2)p_2(\mathbf{y})d\mathbf{y} = -\frac{2\beta(\mathbf{x})\omega^2}{\rho_0 c(\mathbf{x})^4} \int_{D_2} G_{k_2}(\mathbf{x}, \mathbf{y})p_1^2(\mathbf{y})d\mathbf{y}, \quad (29)$$

$$p_2(\mathbf{x}) - \int_{D_3} G_{k_3}(\mathbf{x}, \mathbf{y})(k_3^2(\mathbf{y}) - \bar{k}_3^2)p_3(\mathbf{y})d\mathbf{y} = -\frac{9\beta(\mathbf{x})\omega^2}{\rho_0 c(\mathbf{x})^4} \int_{D_3} G_{k_3}(\mathbf{x}, \mathbf{y})p_1(\mathbf{y})p_2(\mathbf{y})d\mathbf{y}, \quad (30)$$

$$p_4(\mathbf{x}) - \int_{D_4} G_{k_4}(\mathbf{x}, \mathbf{y})(k_4^2(\mathbf{y}) - \bar{k}_4^2)p_4(\mathbf{y})d\mathbf{y} = -\frac{8\beta(\mathbf{x})\omega^2}{\rho_0 c(\mathbf{x})^4} \int_{D_4} G_{k_4}(\mathbf{x}, \mathbf{y})(p_2^2(\mathbf{y}) + 2p_1(\mathbf{y})p_3(\mathbf{y}))d\mathbf{y}, \quad (31)$$

$$p_5(\mathbf{x}) - \int_{D_5} G_{k_5}(\mathbf{x}, \mathbf{y})(k_5^2(\mathbf{y}) - \bar{k}_5^2)p_5(\mathbf{y})d\mathbf{y} = -\frac{25\beta(\mathbf{x})\omega^2}{\rho_0 c(\mathbf{x})^4} \int_{D_5} G_{k_5}(\mathbf{x}, \mathbf{y})(p_1(\mathbf{y})p_4(\mathbf{y}) + p_2(\mathbf{y})p_3(\mathbf{y}))d\mathbf{y}, \quad (32)$$

477 where  $\bar{k}_i$  is the wavenumber of the background medium for harmonic  $i$ , and  $k_i(\mathbf{x})$  is the  
 478 variable wavenumber. Note that the integrals on the left-hand sides have non-zero contribu-  
 479 tions only where  $k_i(\mathbf{x}) \neq \bar{k}_i$ , i.e., where the wavenumber differs from that of the background  
 480 medium. If  $k_i(\mathbf{x}) \equiv \bar{k}_i$ , then we are in the homogeneous case considered before.

481 To validate the rule of thumb for an inhomogeneous medium, we consider a 2cm layer  
 482 of kidney tissue surrounded by water. The layer is centred at the focus of the transducer.  
 483 As the tissue properties for water and kidney, we use those given in Table II, expect that

we assume the density of kidney to be equal to that of water, to coincide with our constant density assumption. We consider the H131 transducer operating at 50W. A comparison with the HITU simulator is presented in Figure 12 where we observe good agreement in terms of focus location as well as magnitudes of the separate harmonics. Since HITU is a one-way solver, it does not approximate the backscattering, whereas our full-wave solver does. The backscattering can be observed as the ripples in the VIE curves.

We note that in the above we assumed that  $\rho(\mathbf{x}) \approx \rho_0$  throughout the inhomogeneous domain. This was done in order to derive convenient volume integral equations, which can be solved in an efficient manner. For strong density contrasts, the VIEs (28)-(32) must be augmented with *boundary integrals*, as discussed in (Costabel, 2015). This complicated could be resolved by a coupling to an established boundary element code, such as (van 't Wout *et al.*, 2015), but this is left to future work.

## VIII. CONCLUSION

In this paper we have set out to reduce the computational burden of numerical schemes for FUS simulations through the construction of an efficient and simple meshing strategy. This strategy can be employed with those numerical schemes that seek to approximate the Westervelt equation on a single non-uniform mesh, and those that solve for each harmonic on separate meshes, such as the frequency-domain volume potential approach proposed here.

The strategy exploits the increasingly localised nature of the higher harmonics around the transducer's focal region so that the degrees of freedom in the mesh can be more efficiently distributed. If we were considering a single non-uniform mesh approach in which we

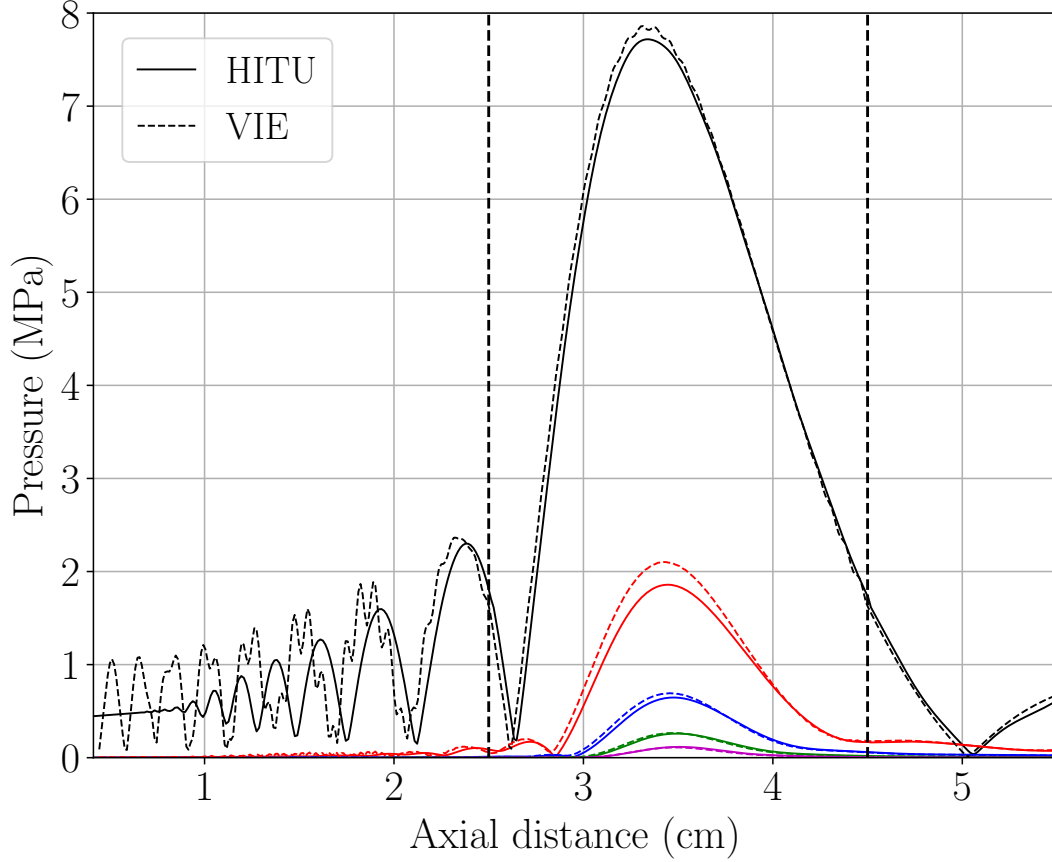


FIG. 12. The on-axis absolute pressure field for the first five harmonics generated by the H131 transducer at 50W in water with a 2cm layer of kidney material centred at 3.5cm. The vertical dashed lines demarcate the kidney layer.

approximate the full Westervelt equation, this mesh would become increasingly more refined toward the focus, since this is where the higher harmonics are present. In the frequency-domain setting we considered, this leads to a nested series of meshes, as was discussed in detail in this article.

In the frequency domain, the Westervelt equation can be rewritten as a series of inhomogeneous Helmholtz equations. When the propagation medium is taken to be homoge-

neous, these Helmholtz equations can be solved exactly by volume potentials, which may be efficiently evaluated using the quadrature method proposed in Section III. This novel application of this approach allow us to explore efficiently the convergence of each harmonic as the respective computation domain was changed in size. Thus enabling us to determine the smallest domains we could use in order to achieve an error of less than 1%.

We showed that the accurate approximation of the second harmonic requires a computation domain that extends from the focus all the way to the transducer, since the first harmonic is not sufficiently localised near the focus to allow a smaller domain to be employed. The third harmonic and above, however, can be approximated accurately on considerably reduced domains. We found that scaling the computation domain’s width and height relative to the wavelength under consideration allowed for accurate approximations for the first five harmonics for the FUS configurations considered here. This leads to a reduction in the number of degrees of freedom of approximately  $(n/2)^3$ , where  $n$  is the number of harmonics being computed.

Finally, we demonstrated how this approach generalises, via the introduction of volume integral operators, to inhomogeneous media with low density variation. The application to inhomogeneous media with large density contrast, such as between water and bone, requires the introduction of further boundary integral operators, with is left to future work.

To conclude, we briefly comment on the generalisation of the ‘rule of thumb’ to other transducer configurations and frequencies. In the present article, two different transducers were considered, both at 1.1MHz, and propagating within three different media: water, liver, kidney. All the examples considered produced peak amplitudes of lower than 15MPa,

at which the weakly nonlinear assumption used in the derivation of the cascade of Helmholtz equations is accurate. We believe that for different focused transducer configurations and frequencies, our proposed rule of thumb is accurate, provided the field can still be categorised as weakly nonlinear. For highly nonlinear fields, a further study would be required to test the ‘rule of thumb’, and also a modification of our volume potential approach required to allow for the transfer of energy from higher to lower harmonics.

A Python implementation of this work is freely available at [github.com/samuelpgroth/vines](https://github.com/samuelpgroth/vines).

## ACKNOWLEDGMENTS

This work was supported by a grant entitled “Optimising patient specific treatment plans for ultrasound ablative therapies in the abdomen (OptimUS)” from the EPSRC (EP/P013309/1 to Cambridge, EP/P012434/1 to UCL).

- Azhari, H. (2010). *Basics of biomedical ultrasound for engineers* (John Wiley & Sons).
- Campos-Pozuelo, C., Dubus, B., and Gallego-Juárez, J. A. (1999). “Finite-element analysis of the nonlinear propagation of high-intensity acoustic waves,” *The Journal of the Acoustical Society of America* **106**(1), 91–101.
- Chen, W., and Holm, S. (2004). “Fractional Laplacian time-space models for linear and nonlinear lossy media exhibiting arbitrary frequency power-law dependency,” *The Journal of the Acoustical Society of America* **115**(4), 1424–1430.
- Colton, D., and Kress, R. (2013). *Integral equation methods in scattering theory*, **72** (SIAM).



- Costabel, M. (2015). “On the spectrum of volume integral operators in acoustic scattering,”  
in *Integral Methods in Science and Engineering* (Springer), pp. 119–127.
- Deserno, M. (2004). “How to generate equidistributed points on the surface of a sphere,” *If  
Polymerforschung* (Ed.) 99.
- Draine, B. T., and Flatau, P. J. (1994). “Discrete-dipole approximation for scattering cal-  
culations,” *The Journal of the Optical Society of America A* **11**(4), 1491–1499.
- Du, Y., and Jensen, J. A. (2013). “Fast simulation of non-linear pulsed ultrasound fields  
using an angular spectrum approach,” *Ultrasonics* **53**(2), 588–594.
- Duck, F. A. (2013). *Physical properties of tissues: a comprehensive reference book* (Aca-  
demic press).
- Frigo, M., and Johnson, S. G. (2005). “The design and implementation of FFTW3,” *Pro-  
ceedings of the IEEE* **93**(2), 216–231 special issue on “Program Generation, Optimization,  
and Platform Adaptation”.
- Gavrilov, L. R., and Hand, J. W. (2000). “A theoretical assessment of the relative perfor-  
mance of spherical phased arrays for ultrasound surgery,” *IEEE Transactions on Ultrason-  
ics, Ferroelectrics, and Frequency Control* **47**(1), 125–139.
- Gélat, P., Ter Haar, G., and Saffari, N. (2011). “Modelling of the acoustic field of a multi-  
element HIFU array scattered by human ribs,” *Physics in Medicine & Biology* **56**(17),  
5553.
- Groth, S. P., Polimeridis, A. G., and White, J. K. (2020). “Accelerating the discrete dipole  
approximation via circulant preconditioning,” *Journal of Quantitative Spectroscopy and  
Radiative Transfer* **240**, 106689.

Gu, J., and Jing, Y. (2015). “Modeling of Wave Propagation for Medical Ultrasound: A Review,” IEEE Transactions on Ultrasonics, Ferroelectrics, and Frequency Control **62**(11), 1979–1992.

Hamilton, M. F., Blackstock, D. T. *et al.* (1998). *Nonlinear acoustics*, **237** (Academic press San Diego).

Izadifar, Z., Babyn, P., and Chapman, D. (2017). “Mechanical and biological effects of ultrasound: A review of present knowledge,” Ultrasound in medicine & biology **43**(6), 1085–1104.

Jaros, J., Rendell, A. P., and Treeby, B. E. (2016). “Full-wave nonlinear ultrasound simulation on distributed clusters with applications in high-intensity focused ultrasound,” The International Journal of High Performance Computing Applications **30**(2), 137–155.

Jones, E., Oliphant, T., Peterson, P. *et al.* (2001–). “SciPy: Open source scientific tools for Python” <http://www.scipy.org/>.

Karzova, M. M., Yuldashev, P. V., Sapozhnikov, O. A., Khokhlova, V. A., Cunitz, B. W., Kreider, W., and Bailey, M. R. (2017). “Shock formation and nonlinear saturation effects in the ultrasound field of a diagnostic curvilinear probe,” The Journal of the Acoustical Society of America **141**(4), 2327–2337.

Khokhlova, T. D., Canney, M. S., Khokhlova, V. A., Sapozhnikov, O. A., Crum, L. A., and Bailey, M. R. (2011). “Controlled tissue emulsification produced by high intensity focused ultrasound shock waves and millisecond boiling,” The Journal of the Acoustical Society of America **130**(5), 3498–3510.

Kinsler, L. E., Frey, A. R., Coppens, A. B., and Sanders, J. V. (1999). *Fundamentals of Acoustics* (Wiley).

Kreider, W., Yuldashev, P. V., Sapozhnikov, O. A., Farr, N., Partanen, A., Bailey, M. R., and Khokhlova, V. A. (2013). “Characterization of a multi-element clinical hifu system using acoustic holography and nonlinear modeling,” *IEEE transactions on ultrasonics, ferroelectrics, and frequency control* **60**(8), 1683–1698.

Marburg, S. (2008). “Discretization requirements: How many elements per wavelength are necessary?,” in *Computational Acoustics of Noise Propagation in Fluids-Finite and Boundary Element Methods* (Springer), pp. 309–332.

Maxwell, A. D., Wang, T.-Y., Cain, C. A., Fowlkes, J. B., Sapozhnikov, O. A., Bailey, M. R., and Xu, Z. (2011). “Cavitation clouds created by shock scattering from bubbles during histotripsy,” *The Journal of the Acoustical Society of America* **130**(4), 1888–1898.

Solovchuk, M., Sheu, T. W., and Thiriet, M. (2013). “Simulation of nonlinear Westervelt equation for the investigation of acoustic streaming and nonlinear propagation effects,” *The Journal of the Acoustical Society of America* **134**(5), 3931–3942.

Solovchuk, M. A., Hwang, S. C., Chang, H., Thiriet, M., and Sheu, T. W. (2014). “Temperature elevation by HIFU in ex vivo porcine muscle: MRI measurement and simulation study,” *Medical physics* **41**(5), 052903.

Soneson, J. (Accessed: 2020-05-06). *HITU Simulator*, <https://www.fda.gov/about-fda/cdrh-offices/hitu-simulator>.

Soneson, J. E. (2017). “Extending the utility of the parabolic approximation in medical ultrasound using wide-angle diffraction modeling,” *IEEE Transactions on Ultrasonics, Fer-*

roelelectrics, and Frequency control **64**(4), 679–687.

Sonic Concepts (**Accessed: 2020-08-19**). *Sonic Concepts transducers*, <https://sonicconcepts.com/transducer-selection-guide>.

Szabo, T. L. (**1994**). “Time domain wave equations for lossy media obeying a frequency power law,” *The Journal of the Acoustical Society of America* **96**(1), 491–500.

Treeby, B. E., and Cox, B. (**2010**). “Modeling power law absorption and dispersion for acoustic propagation using the fractional laplacian,” *The Journal of the Acoustical Society of America* **127**(5), 2741–2748.

Treeby, B. E., Jaros, J., Rendell, A. P., and Cox, B. (**2012**). “Modeling nonlinear ultrasound propagation in heterogeneous media with power law absorption using a k-space pseudospectral method,” *The Journal of the Acoustical Society of America* **131**(6), 4324–4336.

van ’t Wout, E., G  lat, P., Betcke, T., and Arridge, S. (**2015**). “A fast boundary element method for the scattering analysis of high-intensity focused ultrasound,” *The Journal of the Acoustical Society of America* **138**(5), 2726–2737.

Vlaisavljevich, E., Kim, Y., Allen, S., Owens, G., Pelletier, S., Cain, C., Ives, K., and Xu, Z. (**2013**). “Image-guided non-invasive ultrasound liver ablation using histotripsy: feasibility study in an in vivo porcine model,” *Ultrasound in medicine & biology* **39**(8), 1398–1409.

Yuldashev, P., and Khokhlova, V. (**2011**). “Simulation of three-dimensional nonlinear fields of ultrasound therapeutic arrays,” *Acoustical physics* **57**(3), 334–343.